High Sensitivity Spectrograph for Use in Fluorescence Microscopy

P. L. T. M. FREDERIX, M. A. H. ASSELBERGS, W. G. J. H. M. VAN SARK, D. J. VAN DEN HEUVEL, W. HAMELINK, E. L. DE BEER, and H. C. GERRITSEN*

Department of Medical Physiology, Faculty of Medicine, Utrecht University, The Netherlands (P.F., E.d.B.); Department of Molecular Biophysics, Debye Institute, Utrecht University, 3508 TA Utrecht The Netherlands (P.F., M.A., W.v.S., D.v.d.H., H.G.); and Department of Physiology, University of Amsterdam, AMC, The Netherlands (W.H.)

In this paper a versatile, high sensitivity spectrograph is presented for use in fluorescence microscopy. The high sensitivity is achieved by using a prism for the dispersion in combination with a state-of-the-art back illuminated charge-coupled device (CCD) camera. The spectrograph, including the CCD camera, has a detection efficiency of 0.77 ± 0.05 at 633 nm. Full emission spectra with a 1–5 nm spectral resolution can be recorded at a maximum rate of 800 spectra per second. Two applications are shown, in which the spectrograph is fiber-coupled to a commercial confocal laser scanning microscope. In the first example, Förster resonance energy transfer imaging experiments were carried out on double-labeled actin filaments in the *in vitro* motility assay. A 160 × 160 point image was recorded in 1.5 min at 3 ms dwell time per image point. In the second application, a time-resolved study of single quantum dots is presented at 5.2 ms time resolution.

Index Headings: **Fluorescence microscopy; Spectral imaging; Time resolved spectroscopy; IVMA; Quantum dot.**

INTRODUCTION

In this paper a high sensitivity spectrograph is presented for use in fluorescence microscopy. Many applications in fluorescence microscopy require multiple wavelength band detection. Examples include the simultaneous imaging of multiple probes in morphological studies, the quantification of ion concentrations using the ratio of the fluorescence signal in two emission bands imaging,[1] and the measurement of nanometer co-localization by means of Förster resonance energy transfer (FRET).[2,3]

A common and simple way to implement the detection of multiple wavelength bands is the use of multiple emission filters. However, the bandwidth of the emission filters is in general comparatively broad, and the number of wavelength bands used in the imaging experiment is limited. The number of wavelength bands that can be detected simultaneously limits the number of parameters that can be monitored. Importantly, the broad emission bands of fluorescent probes often overlap. This overlap complicates the separation of multiple spectra. Moreover, the broad detection bandwidth and limited number of detection channels do not allow assessment of the shapes of the emission spectra. Therefore, no direct indication of unexpected spectral shifts or the presence of artifacts such as autofluorescence or scattered excitation light is present in the images. This may result in the misinterpretation of the observed intensities.

The measurement of full emission spectra under the microscope can be used to solve these problems.[4–11] However, the acquisition of reliable emission spectra requires the detection of a large number of photons. This restricts both the acquisition rate of the images and the number of images that can be recorded before a dye is photobleached.

In this paper we describe a highly sensitive spectrograph that is optimized for use in (scanning) fluorescence microscopy. The high sensitivity is achieved by using a prism for the dispersion in combination with a back illuminated CCD camera. Full emission spectra with a 1–5 nm resolution can be recorded with millisecond dwell times.

Two examples are presented. In the first example the spectrograph was applied in FRET imaging experiments on double-labeled actin filaments in the *in vitro* motility assay (IVMA). Here, the emission spectra of each pixel were fitted to a superposition of reference dye spectra using a singular value decomposition (SVD) algorithm. The second example concerns a time-resolved study on single (CdSe)ZnS quantum dots. Here, the narrow spectra of two co-localized quantum dots with different emission peaks were followed in time. Both experiments were carried out using a confocal laser-scanning microscope (CLSM).

EXPERIMENTAL

Instrumentation Design. Two important design parameters were the wavelength range and the spectral resolution of the spectrograph. Here, we restricted ourselves to the use of fluorescent probes emitting in the visible wavelength range. In general a spectral resolution of 1–5 nm is sufficient for the recording of fluorescence spectra. Therefore, the design targets for the wavelength range and resolution of the spectrograph were set to 450–750 nm and 1–5 nm, respectively. Furthermore, reasonable spectral imaging acquisition times require short integration times per spectrum. In a scanning microscope, dwell times per image point of up to a few milliseconds were considered acceptable, though sub-millisecond is preferable.

Another important consideration was the detection efficiency of the spectrograph. In fluorescence microscopy experiments only a limited number of fluorescent molecules are available per image point. The numbers may vary between one, in a single molecule experiment, and a few hundred. This limits the number of available photons per time unit. Moreover, photobleaching constrains the number of photons emitted per molecule, and con-

Received 22 December 2000; accepted 22 March 2001.
* Author to whom correspondence should be sent.

0003-7028/01/5508-1005$2.00/0

sequently, the total number of available photons for the experiment is also limited. Finally, a comparatively large number of detected photons is required to record reliable fluorescence emission spectra. The number of available photons is calculated based on 1 to 100 fluorescent molecules per detected volume element. On assuming a fluorescence lifetime of 5 ns and an excitation intensity of two orders of magnitude below saturation, it can easily be shown that about 2–200 $\times$ 10^6 photons are emitted per second.

A realistic estimate of the effects of the collection efficiency of the microscope objective and the transmission of the optics results in an overall efficiency of the microscope of 5%. From these numbers, it follows that about 100–10 000 photons per millisecond are available at the entrance of the spectrograph. The total number of photons emitted per molecule before photobleaching takes place was found to be 3–4 $\times$ 10^4 for a common fluorescent dye such as fluorescein.[12] Using the 5% overall efficiency, this yields a maximum of 1500–2000 photons per fluorescein molecule at the entrance of the spectrograph. From the above estimate it is clear that the detection efficiency of the spectrograph is an important design consideration.

For the wavelength range of interest, we compared the performance of two (2D) detectors, a back illuminated CCD camera (BCCD), and an intensified CCD camera (ICCD). Linear detectors such as photodiode arrays and linear CCDs were omitted from the comparison. In general the linear detectors suffer from a high readout noise level, making them less suitable for low light level spectral imaging. In order to compare the two detectors, the signal-to-noise ratio (S/N) of single detection channels was used as a figure of merit. The S/N of single channels of the CCD was calculated as follows.

In the case of the BCCD, the signal detected in one pixel, S, amounts to $S = I \cdot \eta$, with I the available number of photons and η the quantum efficiency of the detector. The total noise N_{tot} is calculated from the individual noise contributions. Here, the dominant sources of noise are noise due to Poisson statistics in the detected signal ($S^{1/2}$) and the readout noise (N_{RD}) of the detector: $N_{tot} = (S + N^2_{RD})^{1/2}$. The short integration times employed here justify the omission of the dark current in N_{tot}. Hence, S/N = $(I \cdot \eta)^{1/2}/(1 + N^2_{RD}/I \cdot \eta)^{1/2}$, showing that for low I, the readout noise gives a significant reduction of the signal-to-noise ratio. In the case of the ICCD, the signal detected per pixel amounts to $S = G \cdot I \cdot \eta$, with G the gain of the intensifier. Now the dominant sources of noise are noise due to Poisson statistics and the multiplicative noise of the intensifier. The latter increases the noise in the detected signal by a constant factor, F.

The dark current and the readout noise of the detector can be both neglected. The latter assumption is reasonable since the image intensifier amplifies the signal of one detected photon to a level that is well above the readout noise of the CCD camera. N_{tot} can thus be calculated using $N_{tot} = G \cdot (F \cdot I \cdot \eta)^{1/2}$ and the signal-to-noise ratio now becomes S/N = $(I \cdot \eta/F)^{1/2}$. This expression is identical to that of an ICCD with noise free amplification and a reduced, ''effective'', quantum efficiency η/F. For the BCCD we assumed a quantum efficiency of $\eta = 90\%$ and a readout noise of $N_{RD} = 6e^-$. These figures correspond to the quantum efficiency and readout noise of a state-of-the-art commercial BCCD camera at 1 MHz clock frequency of the analog-to-digital converter (Princeton Instruments NTE/CCD 1340). For the ICCD we assumed an effective quantum efficiency $\eta/F = 25\%$.

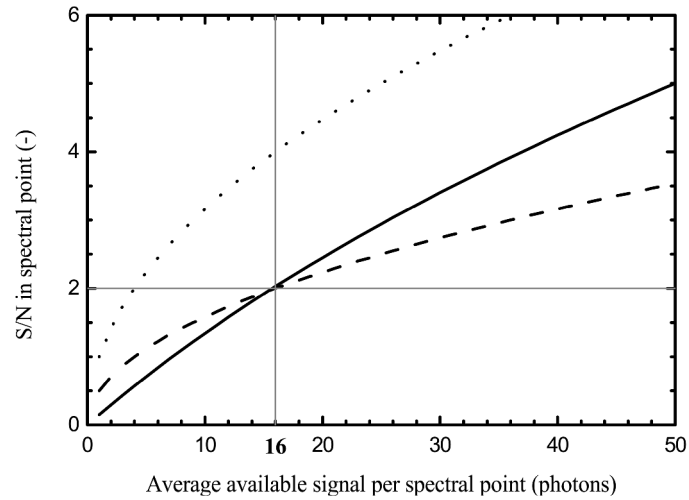

FIG. 1. Signal-to-noise ratios of the detected signal per channel as a function of the number of incident photons. Solid line, BCCD (N_{RD} = $6e^-$ and $\eta = 0.9$); dashed line, ICCD camera ($\eta/F = 0.25$); dotted line, ideal detector. The S/N of the ICCD and the BCCD are equal at 16 incoming photons per channel.

Figure 1 shows the S/N of an ideal detector, $I^{1/2}$ (dotted line), together with that of the BCCD camera (solid line) and of the ICCD camera (dashed line). For signals in excess of 16 incident photons per channel, the BCCD outperforms the ICCD camera. This signal level corresponds to a low S/N of 2. From the sensitivity point of view, the BCCD was most suitable as a detector. Concerning the spectral acquisition rate, BCCDs are generally operated at low readout speeds in order to minimize the readout noise. Using the BCCD described above, spectra can be recorded at a maximum rate of 800 Hz. ICCD cameras can be operated at higher frame rates than BCCDs because the image intensifier reduces the influence of the higher readout noise on the S/N. At higher spectral rates, however, fewer photons are available per spectrum. The lower signal, in combination with the effective quantum efficiency of 25%, makes it questionable whether an ICCD, in practice, will be operated at much higher rates than the BCCD. Based on the above considerations, the BCCD was found to be the best detector for our applications.

Two options were considered for the dispersive element: a grating and a prism. We opted for a prism because only a modest spectral resolution (1–5 nm) is required, it does not suffer from higher order diffraction, and it has high transmission over a broad spectral range. In addition, antireflection (AR) coatings can be used to increase the transmission of the prism. The dispersion of several glass prisms was calculated using the Sellmeier dispersion formula in combination with Snell's law.[13,14] Coefficients for the dispersion formula were extracted from the Schott optical glass catalog. The transmission of the prisms was calculated using the Fresnel equations. The calculations included the interference effects from the single layer AR coating.[13] An AR coated SF10 glass

prism was found to perform well with respect to dispersion and transmission.

Description of the Instrument. ***Spectrograph.*** The spectrograph was designed and constructed in-house, and for flexibility reasons, the entrance of the spectrograph was equipped with an SMA fiber adaptor. Light emerging from the fiber (or directly coupled light) was collimated by a 100 mm *F*/2.5 achromatic lens (Melles–Griot). Next, the light was dispersed by the prism and focused on the CCD camera by an identical lens. Note that the fiber end was projected on the camera without magnification.

An equilateral SF10-glass prism (Linos), operating at minimum deviation conditions, dispersed the light. The lengths of the legs of the prism, as well as the height, were 60 mm. The minimum deviation wavelength was chosen at 550 nm. For this wavelength, the angle of incidence at the entrance surface equaled the angle of emergence at the exit surface. For the prism employed here, this yielded an entrance angle of 60.1°. The interfaces of the prism were coated with a single layer MgF_2 coating to enhance the transmission. The length of the legs of the prism (60 mm) limited the numerical aperture of the spectrograph. The usable prism width was slightly (~1 mm) diminished by the fact that the dispersed beam was wider than the beam before dispersion. From the focal length of the collimating lens and the length of the legs of the prism, a maximum numerical aperture of 0.14 was found for the beam of light entering the spectrograph.

The spectrograph was equipped with a Peltier cooled, back-illuminated CCD camera (Princeton Instruments, NTE/CCD-1340, 16 bit ST133 controller, readout noise $6e^-$ at 1 MHz ADC). The CCD chip was 1340 pixels long in the dispersion direction (horizontal) and 100 pixels high (vertical) and had 20×20 μm^2 square pixels. The spectral measurements were carried out on a small sub-area of the CCD chip of less than 10 pixels high and between 50 and 400 pixels long. The pixels in the direction perpendicular to the dispersion direction were hardware binned. Moreover, hardware binning can also be employed in the dispersion direction, albeit at the price of a loss of spectral resolution. To gain speed, the subarea was positioned at the corner of the CCD chip closest to the readout amplifier. To facilitate alignment of the CCD chip, it was mounted on two orthogonal translation stages. In order to select another wavelength region, the camera was simply translated with respect to the prism.

The examples presented here were all recorded with a confocal laser-scanning microscope (CLSM, Nikon PCM2000, in combination with a Nikon Optiphot 2 microscope). The CSLM scan head was equipped with an FC fiber adapter for excitation and two SMA fiber adapters for coupling the emission light to the remote detectors. The first of the two detection channels was coupled to the spectrograph. A schematic diagram of the setup is shown in Fig. 2. A 50 μm core diameter fiber-patch cord equipped with SMA connectors on both ends (Thorlabs, FG-050-GLA) was used to interface the spectrograph to the CLSM. Because of the comparatively large fiber core diameter of 50 μm, the alignment of the fiber was not critical. The fiber adapter at the CLSM was manually adjusted to optimize the fluorescence signal. Furthermore, the numerical aperture of the light emerging from the CLSM (<0.12) and that of the spectrograph (0.14) were reasonably matched. This ensures efficient coupling of the two devices.

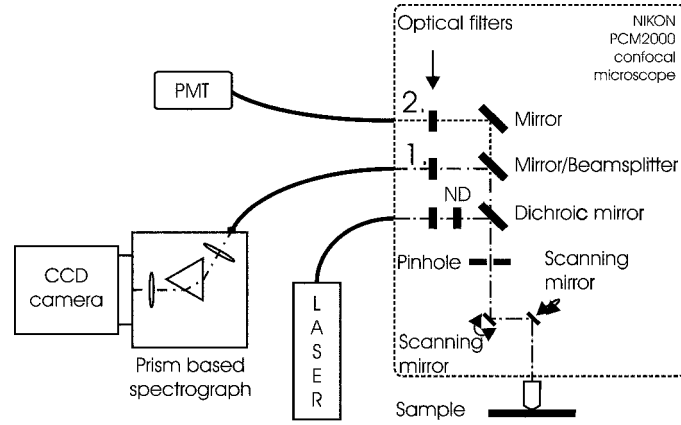

FIG. 2. Schematic overview of the experimental setup. The excitation light from the mixed gas argon-krypton laser is guided to the CLSM by a single mode fiber. An excitation filter and a neutral density filter (ND) can be placed in the excitation beam. Each of the two emission paths can be equipped with a longpass or bandpass emission filter. Detection channel 1 of the CLSM is connected to the spectrograph and channel 2 is connected to a PMT. Channel 1 and 2 are selected by the insertion of a mirror or beamsplitter in the emission path, respectively. The lenses of the CLSM are omitted from the picture for clarity.

The pixel clock pulses generated by the CLSM were used to synchronize the CLSM and the CCD camera controller. The CLSM was used for acquiring 2D spectral images (2D-mode) or for time resolved spectral analysis of small volume elements (time-mode). The wavelength, the confocal pinhole size, the objective magnification, and the numerical aperture of the objective determine the spatial resolution. The measurements discussed below were carried out with a 60 × oil immersion objective (Nikon PlanApo 1.4 NA) and with the larger of two available pinholes (50 μm). The axial and lateral resolutions were estimated to be approximately 1 and 0.3 μm, respectively.

The argon-krypton mixed gas laser (Spectra Physics) used here provides a large number of excitation wavelengths (400–650 nm). A single mode fiber guided the laser light to the CLSM. The excitation light was reflected towards the sample by the built-in dichroic mirrors (Nikon). Typical laser powers at the sample ranged from 1–100 μW.

Performance of the Setup. ***Spectral resolution.*** The main factors determining the spectral resolution of the device are the fiber-core diameter, the dispersion of the prism, the focal lengths of the lenses, and the pixel size of the CCD camera. In addition, the resolution also depends on the number of pixels binned in the dispersion direction. A fiber with a 50 μm fiber-core diameter is used at the input of the spectrograph. It is projected on the CCD without magnification. The projection of the fiber-core on the CCD is larger than the pixel size; monochromatic light spreads out over more than one pixel. Scattered laser light at 476.5, 514.5, and 632.8 nm yielded peaks with a full width at half maximum (FWHM) of 2.2 ± 0.1 pixels in the dispersion direction after binning vertically over 8 pixels. The FWHM is close to the ratio of 2.5 between the fiber-core diameter and the pixel size.

The non-linear spectral bandwidth per camera pixel is

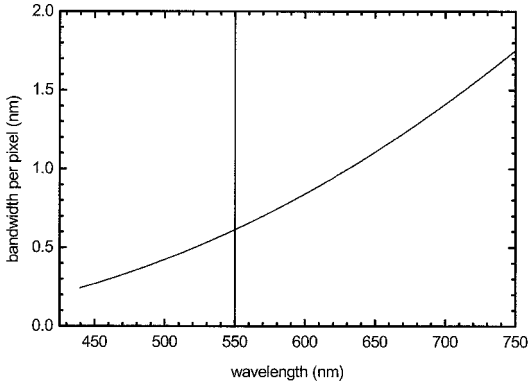

FIG. 3. Pixel bandwidth of the spectrograph, plotted against the wavelength. The vertical line at 550 nm denotes the minimum deviation wavelength of the prism.

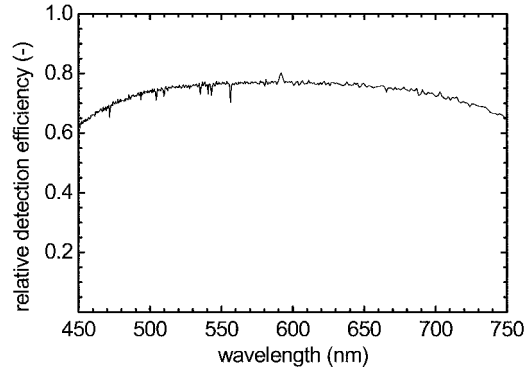

FIG. 4. Detection sensitivity of the spectrograph plus CCD camera for unpolarized light. The light losses due to the fiber are not included in the graph.

calculated using the angular dispersion of the prism,[13] the focal length of the second lens, and the pixel size. Pixel bandwidth is plotted in Fig. 3. In general, the spectral resolution at a specific wavelength can be calculated by multiplying the number of binned pixels by the bandwidth per pixel at that wavelength. However, the projection of the fiber-core on the detector of 2.2 pixels sets a lower limit on the maximum achievable resolution. At wavelengths of 450, 550, and 750 nm a spectral resolution of 1.1, 2.5, and 7.0 nm, respectively, is found using 4 pixel binning.

Detection efficiency. The throughput of the spectrograph (prism plus two lenses) was found to be 0.85 ± 0.05 at 633 nm, which agreed well with the calculations. The quantum efficiency of the CCD camera at this wavelength is approximately $\eta = 0.9$. The overall detection efficiency of the spectrograph plus camera at this wavelength is the product of these two values, and amounts to 0.77 ± 0.05. The shape of the overall detection efficiency curve, now including the fiber, is determined using a calibrated tungsten band lamp. The absolute overall detection efficiency curve is found by normalizing this curve to 0.77 at 633 nm and is shown in Fig. 4. The throughput of the fiber is about 90% and constant within 2.5% in this wavelength range. This is not included in Fig. 4.

Dwell time. The CCD camera has a maximum rate of approximately 800 spectra (20–100 points/spectrum) per second at a $N_{RD} = 6e^-$. Therefore, pixel dwell times in excess of 1.2 ms were employed. In 2D–mode, a 160 × 160 points image with 1.2 ms dwell time is recorded in approximately 40 s. Due to the time lost during the retrace of the mirror, the acquisition time is somewhat longer than the number of spectra multiplied by the dwell time. The internal timing of the camera can be modified to increase the maximum spectral rate at the price of extra noise. Alternatively a slow ADC (100 kHz) can be employed to reduce the N_{RD} to $3.5e^-$. However, this decreases the maximum spectral rate.

Operation. ***Wavelength calibration.*** The spectrograph is operated at a fixed geometry of the prism and lenses. Therefore, the shape of the wavelength calibration curve is constant. This was calculated from the angular dispersion of the prism and the focal length of the lenses. The former was determined using the Sellmeier dispersion formula for SF10 glass (with coefficients taken from the Schott optical glass catalog) in combination with Snell's law.[13,14] The calibration of the spectrograph was accomplished by fitting the measured CCD pixel positions of a number of calibration lines (3 or more) to the theoretical expression of the calibration curve. An additional scaling factor was included to account for errors in the magnification of the spectrograph. The calibration measurements were carried out with laser lines or with a calibration lamp (HgAr lamp, Oriel), depending on the wavelength range of interest. The peak positions were determined using the Winspec-software of the CCD camera (Princeton Instruments). Typically, the calibration accuracy was better than 1 nm over the whole wavelength range.

Data acquisition and processing. Measurements were carried out using two PCs both running Windows 98 (Microsoft). The first PC controls the CLSM and the second controls the CCD camera. The Microsoft automation server and automation manager were used to synchronize the start of the recording of spectra by the CCD camera and the start of the scanning. To this end, the operating software of the CLSM (EZ2000 Nikon, Coord automatisering) was slightly modified. Acquisition of the spectra was carried out using the Winspec-software that controls the CCD camera (Princeton Instruments) and raw data were saved to disk.

For each point in a 2D-image, a whole emission spectrum was recorded. Consequently, 3D data sets were created (x, y, λ). Data processing and visualization of the 3D data sets were carried out with a program written in IDL (Creaso). The program subtracts a user-defined background from the raw spectra and corrects for the detection efficiency of the setup. The wavelength calibration was performed as explained above. Where possible, the average spectrum from an area in the image with no obvious fluorescence was employed as a background. If such an area was not available, a background spectrum from a comparable reference specimen was used. The wavelength dependency of the detection efficiency of the complete setup was corrected for with a 'flatfield' spectrum. The flatfield spectra were determined by using a calibrated tungsten band lamp. The band lamp spectrum was assumed to be identical to the spectrum of a black body radiator of the same temperature. The flatfield spectrum was calculated from the ratio of the band lamp spectrum

to the spectrum of the black body radiator. The flatfield spectrum also includes the variable bandwidth per CCD pixel. Intensity images can be viewed at each recorded wavelength band. Furthermore, emission spectra from selected pixels, or regions of interest, can be viewed and exported for further analysis.

The data sets in time-mode are 2D (t, λ). The processing of these data sets was done as described before. The background was taken from time laps with no obvious fluorescence. If this was not available, a background spectrum from a comparable reference specimen was used.

In the measurements on the *in vitro* motility assay (IVMA), the spectrum of each image point was expressed as a linear combination of reference spectra of the individual probes. The fitted amplitude of each of the components quantifies their contributions to the spectrum. The reference spectra of the probes were recorded in IVMAs under circumstances identical to the multi-component samples. The IVMAs contained only filaments that were either donor or acceptor labeled. To obtain the reference spectra, spectra of several filaments were averaged and normalized on their integral intensity. A standard IDL procedure, based on singular value decomposition (SVDC),[15] was used to decompose the measured spectra of a multi-component IVMA into the reference spectra. The background was subtracted from the spectra before fitting.

Sample Preparation. ***In vitro motility assay.*** The *in vitro* molecular interaction between actin filaments (F-actin) and (subfragments of) myosin can be studied in the *in vitro* motility assay (IVMA). The sample preparations and construction of the IVMA were described previously by Hamelink et al.[16] We immobilized myosin subfragment HMM (Heavy Mero-Myosin, prepared with Chymotrypsin) on a glass slide and added phalloidin-stabilized, labeled actin filaments to form rigor complexes with the HMM. The actin filaments were either labeled with alexa-488 (at phalloidin), with tetramethyl-rhodamine (TMR) (at cys374), or double labeled with both alexa-488 and TMR. Here, the alexa-488 and TMR in the double-labeled filaments serve as donor and acceptor, respectively, for FRET experiments. The iodoacetamide-derivative of TMR (Molecular Probes) was covalently attached to cys374 of the actin, using the recipe given by Trayer and Trayer.[17] Buffers were exchanged in a PD10 column (Amersham Pharmacia Biotech), and excess of buffer was removed with a centrifugal filter device (Centrikon YM-10, Millipore). Acceptor labeled filaments were stabilized with unlabeled phalloidin (Sigma); for donor and double labeled filaments, alexa-488 labeled phalloidin was employed (Molecular Probes). An oxygen scavenger system was added to the buffer solutions shortly before use. The oxygen scavenger was based on the recipe given by Kishino and Yanagida[18] and was added at 3 mg/ml glucose, 21 units/ml glucose oxidase, and 300 units/ml catalase. The Förster distance, as calculated from the spectra of alexa-488 and TMR, equals 6.1 nm, assuming an orientation factor $\kappa^2 = 2/3$, and a quantum efficiency 0.75 for alexa-488. The distances between the two labelling sites were calculated using the coordinates of cys374 and the probe binding site of phalloidin in F-actin, as published by Lorenz et al.[19] The distances of the four closest acceptor sites from a donor site are within the Förster distance. Therefore, a significant energy transfer efficiency is expected in double-labeled actin filaments.

Quantum dots. Semiconductor quantum dots (QDs) are a promising alternative for fluorescent probes in microscopy.[20,21] The QDs are generally a few nanometers in diameter. Interestingly, the emission wavelength of the QD increases with the size.[22] An important advantage of QDs is the narrow (typically 15 nm FWHM), Lorentzian shape of their emission spectrum. The emission spectrum of the QD lacks the long red tail commonly found in organic dyes. As a result, multiple differently sized quantum dots can be easily separated spectrally.[10] The excitation bands, on the other hand, are very broad; therefore, quantum dots with different emission bands (diameter) can all be excited at the same wavelength. Moreover, the broad excitation spectrum allows excitation far away from the emission band, thus introducing a large Stoke's shift. Finally, quantum dots are photo-stable and exhibit only modest photobleaching. However, QDs sometimes show a strong blinking behavior that is less favorable for microscopic applications. The QDs employed here are CdSe dots with a ZnS capping for passivation. The (CdSe)ZnS QDs were synthesized according to a slightly modified method as described by Hines and Guyot–Sionnest.[23] Chloroform dispersed QDs were spread on a coverslide and dried in air prior to mounting in the setup.

Applications. All the example experiments described herein were carried out with the CLSM. Areas of interest were previewed and selected using the standard PMT of the CLSM (detection channel 2 in Fig. 2). All emission light was directed to the spectrograph detection channel 1 when acquiring spectra. Although scattered laser light is spectrally separated from the fluorescence emission, it may introduce artifacts in the spectra, particularly close to the excitation wavelength. Therefore, both detection channels were equipped with emission filters to suppress scattered excitation light. In the 2D-mode, images of 160 $\times$ 160 points were acquired, with a field of view of 32 $\times$ 32 μm^2. In the time-mode, the scanning mirrors are parked at the position of interest during the acquisition of the spectra.

In vitro motility assay. The FRET study on the *in vitro* motility assay was carried out in the 2D-mode. The IVMA contained three differently labeled actin filaments: donor labeled, acceptor labeled, and donor plus acceptor labeled. We employed 488 and 531 nm laser light for the direct excitation of alexa-488 and TMR, respectively. However, the TMR molecules have some residual absorption at 488 nm. Figure 5A shows the integral emission intensity between 500 and 700 nm of the IVMA, at 488 nm excitation. A 500 nm longpass filter (Chroma, HQ500LP) was inserted in detection channel 1 to block scattered laser light (see Fig. 2). The spectra were recorded with a 3 ms dwell time per image point, and the total acquisition time for an image amounted to 1.5 min. Eight-pixel binning was employed in the spectral direction, yielding a spectral resolution of approximately 5 nm at 550 nm.

Figure 6 shows emission spectra from three single image points in the image. The position of the image points are indicated by the arrows in Fig. 5A. The spectra of a

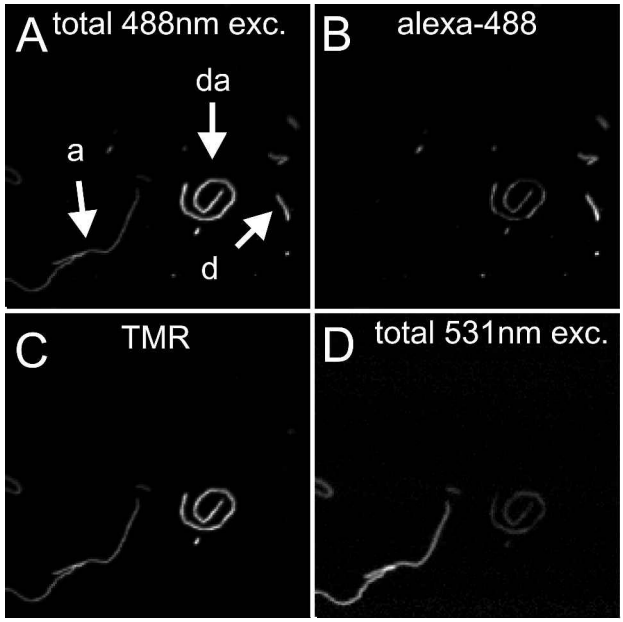

FIG. 5. Spectral data from an IVMA containing a mixture of 3 differently labeled actin filaments: only donor (alexa-488 at phalloidin), only acceptor (TMR at cys374) and both donor and acceptor labeled filaments. (**A**) Integral emission intensity between 500 nm and 700 nm at 488 nm excitation. The arrows indicated by *d, a* and *da* point to donor, acceptor, and double labeled filaments, respectively. (**B**) Fitted contribution of alexa-488, (**C**) fitted contribution of TMR, and (**D**) Integral intensity at 531 nm to directly measure the TMR density of the filaments. Spectra of three different pixels in the image are plotted in Fig. 6.

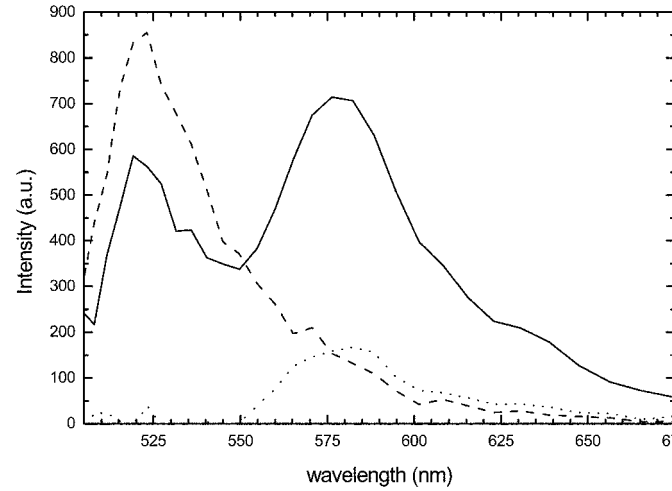

FIG. 6. Single pixel spectra from actin filaments in Fig. 5. Dashed line: filament labeled with donor only; dotted line: filament labeled with acceptor only; and solid line: filament labeled with both donor and acceptor. The background is subtracted from the spectra and the spectra are flatfield corrected.

donor only, acceptor only, and a donor plus acceptor labeled filament are represented by the dashed, dotted, and solid lines, respectively. In the donor plus acceptor spectrum, a large acceptor enhancement is visible in combination with a donor signal reduction with respect to the spectra of the single labeled filaments. The spectra at each image point were analyzed by using the SVD method. The spectra of alexa-488 and TMR were used as references. Although there is some spectral overlap between the emission of alexa-488 and TMR, fitting the full spectra yields the contributions of the two probes without any cross talk. Figures 5B and 5C show the contributions of the two probes in each image point. The donor only and acceptor only labeled filaments appear exclusively in image B and C, respectively. The double-labeled filaments, however, appear in both image B and C. In agreement with the spectra of Fig. 6, the donor plus acceptor labeled filaments show a clear acceptor enhancement in Fig. 5C. Moreover, the same filaments show a donor signal reduction in Fig. 5B.

To show that the enhanced TMR intensity in the double-labeled filament was indeed caused by FRET and not by a higher TMR density, a second spectral image was recorded at an excitation wavelength of 531 nm. The integrated emission intensity of this image is shown in Fig. 5D. The image was recorded with the same spectral resolution and dwell time as before, but now using a 545 nm longpass filter to block scattered laser light. At the 531 nm excitation wavelength alexa-488 does not show any significant absorption. However, TMR possesses strong absorption bands at this wavelength. For this reason, the emission intensity at this excitation wavelength is a direct measure of the TMR density in the filament. The double-labeled filaments do not show higher TMR intensities than the filaments labeled with TMR only, but rather a lower intensity. This indicates that the probe density of TMR is not higher in the double-labeled than in the acceptor-only labeled filaments. These findings, in combination with the enhanced acceptor intensity of the double-labeled filaments in Fig. 5C unambiguously prove the occurrence of FRET between alexa-488 and TMR in the double-labeled actin filaments. The occurrence of FRET was confirmed by other experiments in which photobleaching of the TMR yielded an increase in the alexa-488 signal (data not shown). The lower TMR intensity at 531 nm excitation of the double-labeled filament with respect to the single-labeled filament is explained by energy transfer sensitized photobleaching during the preceding 488 nm excitation experiment.[24] This was confirmed by reversing the recording sequence of the images at the two excitation wavelengths (data not shown). In this case the TMR fluorescence of the single- and double-labeled filaments did not differ at 531 nm excitation.

Quantum dots. The experiments on single quantum dots were carried out in the time-mode of the spectrograph. The quantum dots were excited at 468 nm and the emission was detected between 500 nm and 700 nm. Four pixels were binned in the spectral direction, yielding a ~3 nm spectral resolution at 580 nm, and a 5.2 ms integration time per spectrum was employed. A 480 nm longpass filter (Ba480, Nikon) was inserted in the detection path to block scattered laser light. A 1 s time trace, out of a 3 min recording, is plotted in Fig. 7. Here, the wavelength is plotted vertically and the time horizontally. Two horizontal bands are visible, showing the presence of two quantum dots, co-localized in the detection volume. The upper and lower bands correspond to two quantum dots with emission maximums at 610 nm (quantum dot 1) and 555 nm (quantum dot 2). Figure 8 shows the spectra at three different points in time; the three arrows in Fig. 7 indicate the positions of the spectra. At position I, only quantum dot 1 is emitting; at position II, only

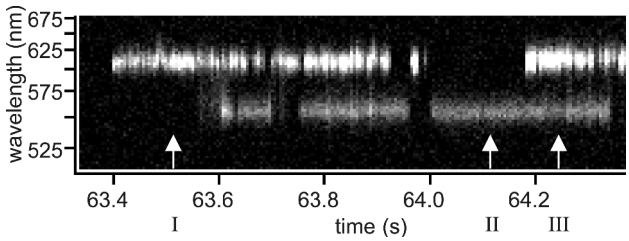

FIG. 7. Time-resolved emission spectra of two co-localized quantum dots at 5.2 ms dwell time per spectrum. The wavelength is plotted vertically, and the time is plotted horizontally. The emission maximums of the two quantum dots are at 610 and 555 nm for quantum dots 1 and 2, respectively. The three arrows mark positions where only dot 1 is emitting (I), dot 2 is emitting (II), or both dots are emitting (III). The spectra at these points are shown in Fig. 8.

quantum dot 2 is emitting; and at position III, both dots are emitting. Quantum dot 1 has a higher emission intensity than quantum dot 2. For an extensive description and discussion of these experiments we refer to van Sark et al.[25]

CONCLUSION

In this paper we describe a sensitive spectrograph that is optimized for use in (scanning) fluorescence microscopy. The most critical design parameter is the overall sensitivity of the spectrograph in the wavelength range 450–750 nm. In order to compare the sensitivity of the detectors, the S/N per detection channel was used as a figure of merit. Two detectors were compared, a BCCD and a sensitive ICCD. For the BCCD, the specifications of the Princeton Instruments NTE/CCD-1340 were used, and for the ICCD the specifications of a fictive camera equipped with a fourth generation image intensifier were used.

The effective quantum efficiency of the ICCD was chosen to be $\eta/F = 0.25$. This is lower than the quantum efficiency specified for commercially available Gen IV image intensifiers. For these intensifiers, peak η values in excess of 40% are given. However, a thin protective layer between the photo-cathode and the front side of the micro-channel plate of the image intensifier reduces the overall quantum efficiency of the ICCD. The protective layer serves to prevent ion feedback, but also blocks 20–30% of the photoelectrons. Furthermore, the sensitivity of the ICCD is affected by multiplicative noise. A realistic value of the noise factor related to this type of noise is $F \approx 1.4$.[26] Therefore, an effective quantum efficiency of 25% seems reasonable for the ICCD system. It should be noted that image intensifiers are employed for fast shuttering.[7] This offers the possibility of recording spectra with nanosecond time resolution.

A single layer AR coated prism was chosen to disperse the light. This yields a high transmission of about 85% and can be further improved by applying a custom multilayer AR coating. A disadvantage of a prism compared to a grating is the larger non-linearity in the dispersion. This, however, can be easily corrected for and does not restrict the applicability of the spectrograph. The fiber coupling introduces extra light losses (about 10–15%) compared to direct coupling of the emission light into the spectrograph. The fiber coupling, however, makes the

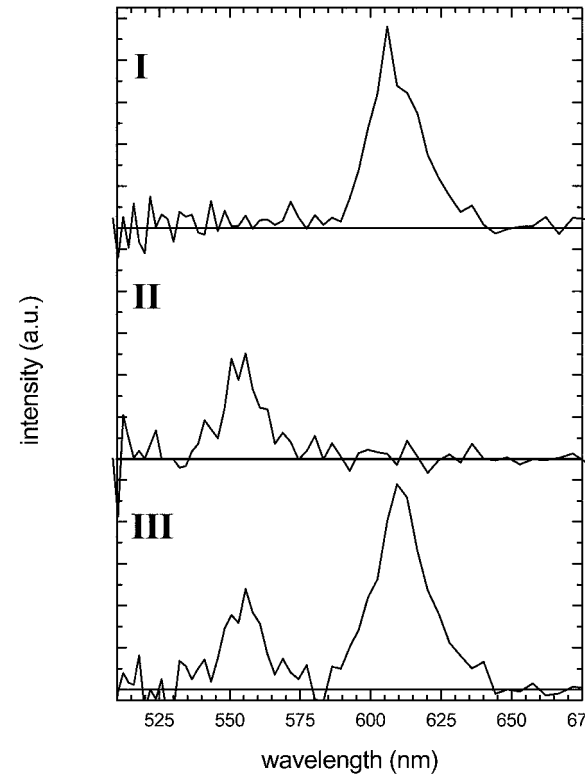

FIG. 8. Three spectra taken from the time trace of Fig. 7: (I) only quantum dot 1 emitting, (II) only quantum dot 2 emitting, and (III) both dots emitting.

spectrograph very versatile. The throughput of the fiber can be improved by coating the faces of the fiber. The spectrograph records only one spectrum, with a limited number of points at a time. Therefore, only a small section of the CCD chip is employed for the recording of spectra with millisecond acquisition times. Often the full size of the CCD chip is used.[4,6,7,8] Here, the direction on the chip perpendicular to the dispersion direction contains spatial information of the sample. This allows for faster recording of the spectra from a complete line in the sample; however, longer readout times are required to read out the chip. In general, the gain in acquisition speed for a complete 2D image will be limited. Moreover, this configuration does not allow for fast (millisecond) time resolved measurements.

Although an ADC speed of 1 MHz was employed, we could not operate the camera at spectral rates above 800 Hz. This was somewhat surprising because the spectra contained only about 100 points. This is much lower than expected based on the speed of the ADC. The difference is explained by the overheads in the readout timing, e.g., dummy reads and software delays. The setup can be used in 2D-mode or in time-mode, and we showed applications of each of the acquisition modes. In the 2D-mode, a 160 × 160 pixel image was collected in 1.5 min. The spectra of alexa-488 and TMR show significant overlap. Decomposition of the acquired spectra reveals the contributions of the two probes to the spectrum, with negligible cross talk. The spectra unambiguously revealed energy transfer between alexa-488 and TMR in the double-labeled filaments. The measurements showed some photobleaching of the TMR. However, spectra of suffi-

cient quality can be recorded with much less signal than in Figs. 5 and 6. Consequently, the effects of photobleaching can be significantly reduced. Negligible photobleaching is important for quantification of the energy transfer efficiency.

In the second application, time-resolved spectra of two co-localized quantum dots were recorded. The two quantum dots could be spectrally resolved and their spectra could be followed in time for several minutes with a resolution of 5 ms. Another appealing application of the time resolved recording of spectra is the determination of Ca^{2+} and other ions by means of fluorescence emission ratio imaging.[1] Using the spectrograph this can be accomplished with millisecond time resolution.

The spectrograph presented here is a versatile device that can be employed for many applications. At present, the time resolution is about 1.2 ms and limited by the CCD camera. Optimization of the system should enable sub-millisecond acquisition of spectra. Furthermore, the sensitivity of the system can be somewhat improved by employing an optimized coating on the prism and fiber faces.

ACKNOWLEDGMENTS

The authors wish to thank A. Meijerink, A. A. Bol, and J. N. J. van Lingen (Debye Institute, Utrecht University) for the kind gift of (CdSe)ZnS quantum dots and for the fruitful discussions. The authors also gratefully acknowledge B. W. Treijtel (Department of Physiology, AMC, University of Amsterdam) and Coord automatisering for technical support and the Netherlands Council for Earth and Life Sciences (ALW) of the Netherlands Organization for Scientific Research (NWO) for financial support.

1. R. Y. Tsien and M. Poenie, Trends Biochem. Sci. **11,** 450 (1986).
2. L. Matyus, J. Photochem. Photobiol., B **12,** 323 (1992).
3. G. W. Gordon, G. Berry, X. H. Liang, B. Levine, and B. Herman, Biophys. J. **74,** 2702 (1998).
4. A. Feofanov, S. Sharonov, P. Valisa, E. Da Silva, I. Nabiev, and M. Manfait, Rev. Sci. Instrum. **66,** 3146 (1995).
5. J.-M. Millot, L. Pingret, J.-F. Angiboust, A. Bonhomme, J.-M. Pinon, and M. Manfait, Cell Calcium **17,** 354 (1995).
6. R. Martínez-Zaguilán, M. W. Gurulé, and M. Lynch, Am. J. Physiol. **270,** C1438 (1996).
7. G. Vereb, E. Jares-Erijman, P. R. Selvin, and T. M. Jovin, Biophys. J. **74,** 2210 (1998).
8. C. Favard, P. Valisa, M. Egret-Charlier, S. Sharonov, C. Herben, M. Manfait, E. Da Silva, and P. Vigny, Biospectroscopy **5,** 101 (1999).
9. L. Rigacci, R. Alterini, P. A. Bernabei, P. R. Ferrini, G. Agati, F. Fusi, and M. Monici, Photochem. Photobiol. **71,** 737 (2000).
10. T. D. Lacoste, X. Michalet, F. Pinaud, D. S. Chemla, A. P. Alivisatos, and S. Weiss, PNAS **97,** 9461 (2000).
11. H. Tsurui, H. Nishimura, S. Hattori, S. Hirose, K. Okumura, and T. Shirai, J. Histochem. Cytochem. **48,** 653 (2000).
12. R. Y. Tsien and A. Waggoner, in *Handbook of Biological Confocal Microscopy,* J. B. Pawley, Ed. (Plenum Press, New York 1995), Chap. 16.
13. M. Born and E. Wolf, *Principles of Optics* (Cambridge University Press, Cambridge 1999), 7th ed.
14. E. Hecht, *Optics* (Addison–Wesley, 1987), 2nd ed.
15. W. H. Press, B. P. Flannery, S. A. Teukolsky, and W. T. Vetterling, *Numerical Recipes in Pascal,* (Cambridge University Press, Cambridge, 1994).
16. W. Hamelink, J. G. Zegers, B. W. Treijtel, and T. Blangé, Anal. Biochem. **273,** 12 (1999).
17. R. H. Trayer and I. P. Trayer, Biochemistry **27,** 5718 (1988).
18. A. Kishino and T. Yanagida, Nature **334,** 74 (1988).
19. M. Lorenz, D. Popp, and K. C. Holmes, J. Mol. Biol. **234,** 826 (1993).
20. M. Bruchez, Jr., M. Moronne, P. Gin, S. Weiss, and A. P. Alivisatos, Science **281,** 2013 (1998).
21. W. C. W. Chan and S. Nie, Science **281,** 2016 (1998).
22. B. O. Daboussi, J. Rodriguez-Viejo, F. V. Mikulec, J. R. Heine, H. Mattoussi, R. Ober, K. F. Jensen, and M. G. Bawendi, J. Phys. Chem. B **101,** 9463 (1997).
23. M. A. Hines and P. Guyot-Sionnest, J. Phys. Chem. **100,** 468 (1996).
24. V. M. Mekler, A. Z. Averbakh, A. B. Sudarikov, and O. V. Kharitonova, J. Photochem. Photobiol., B **40,** 278 (1997).
25. W. G. J. H. M. van Sark, P. L. T. M. Frederix, D. J. van den Heuvel, M. A. H. Asselbergs, I. Senf, and H. C. Gerritsen, Single Molecules **1,** 291 (2000).
26. M. Stanton, W. Phillips, Y. Li, and K. Kalata, J. Applied Crystallography **25,** 638 (1992).